RSC Advances

PAPER

View Article Online
View Journal | View Issue

Cite this: *RSC Adv.*, 2022, **12**, 25711

Photodegradation of 2,4-D (dichlorophenoxyacetic acid) with Rh/TiO_2; comparative study with other noble metals (Ru, Pt, and Au)

G. A. Reguero-Márquez,[a] M. A. Lunagómez-Rocha,[a] A. Cervantes-Uribe,[a] G. del Angel,[b] I. Rangel,[b] J. G. Torres-Torres,[a] F. González,[b] S. Godavarthi,[c] J. C. Arevalo-Perez,[a] A. E. Espinosa de los Monteros[a] and A. A. Silahua-Pavon*[a]

In this work the effect of noble metal on the photodegradation of 2,4-dichlorophenoxyacetic acid herbicide using TiO_2 as support was studied. The metals and concentration were: Rh, Ru, Pt and Au and 1, 0.98, 1.89, and 1.91 wt% respectively. Rhodium was taken as reference for this experiment. The samples were characterized by X-Ray Diffraction (XRD), UV-vis absorption spectra, N_2 physisorption (BET Specific Surface Area), High Annular Angle Analysis Darkfield (HAADF) and Transmission Electron Microscopy Scanning (STEM), H_2 chemisorption, optical emission spectroscopy with inductive coupling plasma analysis (ICP-OES), solid fluorescence, X-ray Photoelectron Spectroscopy (XPS) and OH quantification. The presence of the anatase crystalline phase was mostly confirmed in all samples. The band gap decreased with the presence of metal (from 3.24 to 2.92 eV). The specific area was a function of the metal particle size. The metal particle diameter showed the following sequence Pt > Ru > Au > Rh. By XPS, TiO_2 does not manifest changes in oxidation states, but when impregnated with metals, only Pt shows the highest abundance of any oxidized state (Pt^{2+}). The presence of metal reveals less electron–hole recombination compared with titanium oxide. The results of photocatalytic activity showed that Pt and Rh are the two metals with the highest mineralization (99.0 and 98.3%, respectively).

Received 8th June 2022
Accepted 2nd September 2022

DOI: 10.1039/d2ra03552a

rsc.li/rsc-advances

Introduction

2,4-Dichlorophenoxyacetic acid is one of the most widely used herbicides in the world due to its mobility and high persistence in soil and water, it is commonly used for the control of broadleaf weeds in gardens, pastures, wheat, rice, and citrus crops, among others.[1] Due to its constant use, it has been possible to quantify and identify it in surface and groundwater due to its low absorption in the soil, high leaching, and medium solubility in water (900 mg L^{-1}).[2] This herbicide has been classified as a possible human carcinogen and is an endocrine disruptor that also affects the central and peripheral nervous system.[3] Therefore, its application has been legislated in many countries to control its use, the Environmental Protection Agency established 70 μg L^{-1} and in Mexico the Ministry of Health established 30 μg L^{-1} as the maximum permissible limits of this substance in water for human consumption.[4–6] Many processes have been developed to remove this pollutant from the aqueous medium, including physical methods such as adsorption;[7] chemical methods such as heterogeneous photocatalysis[8] and biological methods, such as biodegradation.[9] Heterogeneous photocatalysis, compared to other degradation processes, is a more efficient process because it is not a selective method, it is capable of oxidizing and mineralizing persistent organic compounds at low concentrations, it is stable to changes in pH and temperature, and it has low operating costs.[10] However, this process uses a semiconductor. Titanium dioxide (TiO_2) is an important multifunctional semiconductor, which can be applied to energy storage, solar cells, gas sensors, and photocatalysis.[11–13] Generally, TiO_2 in photocatalysis is activated by the adsorption of sufficient radiant energy to overcome the semiconductor's band gap energy (3.2 eV) and generate electron–hole pairs, the latter are responsible for directly oxidizing organic compounds or generating hydroxyl radicals (OH*) in water. Meanwhile, the electrons are responsible for reducing the oxygen present in the medium. The efficient separation of these pairs induces an efficient photocatalytic process, this can be done by modifying the structure and morphology of TiO_2 by adding impurities or other metal oxides

[a]*Universidad Juárez Autónoma de Tabasco, Laboratorio de Nanomateriales Catalíticos Aplicados al Desarrollo de Fuentes de Energía y de Remediación Ambiental, Centro de Investigación de Ciencia y Tecnología Aplicada de Tabasco (CICTAT), DACB, Km. 1 Carretera Cunduacán-Jalpa de Méndez AP. 24, C. P. 86690, Cunduacán, Tabasco, Mexico. E-mail: adib.silahua@ujat.mx; adibab45@gmail.com*

[b]*Universidad Autónoma Metropolitana-Iztapalapa, Departamento de Química, Área de Catálisis, CBI, Av. San Rafael Atlixco No. 186, CP 09340, México DF, Mexico*

[c]*Investigadoras e Investigadores por México-Universidad Juárez Autónoma de Tabasco, Centro de Investigación de Ciencia y Tecnología Aplicada de Tabasco (CICTAT), DACB, Laboratorio de Nanomateriales Catalíticos Aplicados al Desarrollo de Fuentes de Energía y Remediación Ambiental, Km.1 carretera Cunduacán-Jalpa de Méndez, C. P. 86690 Cunduacán, Tabasco, Mexico*

on its surface.[14] Recently the sol–gel method has often been used to prepare and modify the properties of titania such as surface area, crystalline phase distribution, crystal size and band gap energy, the latter when transition metal dopants are added, to increase photoactivity, generating a double effect: decreasing the band gap energy and trapping electrons to avoid electron–hole recombination.[15,16] On the other hand, the incipient impregnation preparation method has become the ideal complement to deposit ions on the TiO_2 surface to remove aqueous contaminants. The impregnation of TiO_2 with noble metal ions such as Pt,[17] Ag,[18] Au (ref. 19) Ru (ref. 20) *y* Pd (ref. 21) in oxidized state is reported in the literature. Other catalyst synthesis methods, such as deposition–precipitation, have proven to be effective in surface insertion and dispersion of these ions in the metallic state.[22] Recently, yolk–shell type nanostructured materials of TiO_2 with noble metals such as Au have been generated, which demonstrate photocatalytic properties.[23] Rh doping of TiO_2 has emerged as a viable technique to enhance visible light absorption. Both Rh^{3+} and Rh^{4+} introduce sub bands in the TiO_2 bandgap. Rh^{3+} contributes a donor level to the valence band, thus reducing the energy of the band and shifting the absorption of light to the visible region.[24] There is little evidence of studies carried out with Rh, among these works are Rh–In_2O_3.[25] where oxytetracycline was degraded; Rh/TiO_2, synthesized by sol–gel, however, the results obtained were not better than TiO_2 in the degradation of *p*-nitrophenol; 2.5% Rh/TiO_2 (ref. 26) modified with HCP by the sol–gel method (dealuminated clinoptilolite) in the degradation of pentachlorophenol.[27] Recent developments indicate that the combination of both metal and semiconductor can be an even better catalyst for harvesting the sola or UV energy compared with those individual components. These combined materials, widely known as heterostructure materials, can retain the properties of the individual entities or generate new properties when placed together within a proximity.[28–30] Therefore, in this work the degradation and mineralization of 2,4-diclophenoxyacetic acid was investigated using photocatalysts of TiO_2 impregnated with 1% Rh, comparing them with Au, Pt, and Ru in the metallic state, respectively, with the same molar ratio, under UV irradiation, to know the effect generated by the Rh ions in the metallic state in the photocatalytic activity with the TiO_2.

Results and discussion

(a) BET specific surface area

The results of the specific area for each material analysed are shown in Table 2. It is observed that when Ti is impregnated with the different metals, this parameter does not undergo significant changes, despite the concentration of platinum greater than 1% by weight, there are no significant changes in the surface area of the titania.[31] However, for this case, the material with Pt manifests a drastic drop in specific area, possibly due to poor dispersion and the growth of metallic agglomerates on the TiO_2 surface.

(b) ICP-analysis

The loaded metal content on the TiO_2 support was determined by ICP-OES measurement. For this work, the amount of metal deposited were: 1, 0.98, 1.89, and 1.91% by weight for Rh, Ru, Pt, and Au, respectively, on the TiO_2 surface. The ICP-OES results (Table 2) suggest that the amount of metal deposited is close to the expected theoretical values.

(c) X-ray diffraction

In Fig. 1, the X-ray diffraction patterns of all the materials are observed, the signals corresponding to the crystalline phases

Table 1 Relative abundance of the different species obtained from XPS data for RhTi, RuTi, PtTi and AuTi catalysts

	Oxidation states											
	Ti		Rh		Ru		Pt			Au	O		
Catalyst	Ti^{3+}	Ti^{4+}	Rh°	Rh^{3+}	Ru°	Ru^{4+}	Pt°	Pt^{2+}	Pt^{4+}	Au°	O_I	O_{II}	O_{III}
TiO_2	3.1	96.9	—	—	—	—	—	—	—	—	88.2	9.9	1.9
Rh/TiO_2	5.5	94.5	54.4	45.6	—	—	—	—	—	—	87.3	10.6	2.1
Ru/TiO_2	5.9	94.1	—	—	84.2	15.8	—	—	—	—	91.1	7.7	1.2
Pt/TiO_2	5.3	94.7	—	—	—	—	56.5	24.9	18.7	—	87.1	10.7	2.2
Au/TiO_2	5.7	94.3	—	—	—	—	—	—	—	100	88.8	9.7	1.5

Table 2 Average metal particle size, crystal size, bandgap energy and activation wavelength, kinetic constant and half-life

Catalyst	E_g (eV)	Surface specific area (BET, $m^2\ g^{-1}$)	λ (nm)	ICP (wt%)	D (%)	$\bar{d}$ (nm)	S_{CO_2}	$K_{app} \times 10^2$ (min^{-1})	$t_{1/2}$ (min)
Ti	3.24	68	382.7	—	—	—	74.3	0.38	182
RhTi	3.10	64	400.0	1.28	69	1.6	98.3	1.13	61
RuTi	3.31	62	424.7	1.22	63	3.3	80.6	0.86	80
PtTi	3.09	42	401.3	2.15	14	8.3	99.0	1.16	59
AuTi	3.18	63	389.9	2.16	53	2.2	98.0	0.94	73

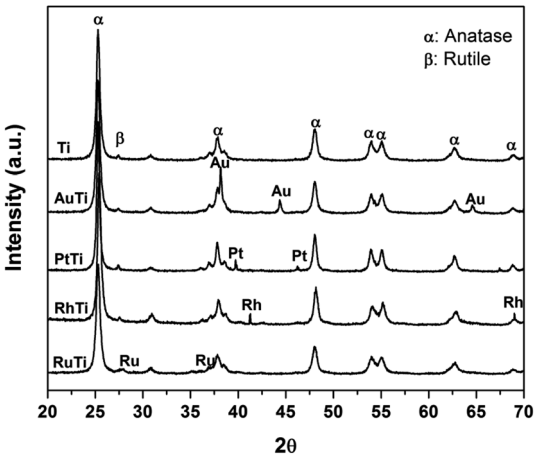

Fig. 1 X-ray diffraction patterns for Ti, AuTi, PtTi, RhTi photocatalysts, and where α = anatase and β = rutile.

anatase (25.3, 37.1, 48.2, 53.1 55.1, 62.2 and 67.61°) and rutile (27.2°) on the 2θ scale for TiO_2 are indicated. The crystal structures were identified by means of the Joint Committee on Powder Diffraction Standards (JCPDS) library, for both phases (anatase 21-1272 and rutile 88-1175). On the other hand, the signals, characteristic of the metals impregnated in the titania were identified: 38.2, 44.4° (Au); 39.8, 46.2° (Pt); 41.1, 69.9° (Ru) and 38.4, 42.2° (Rh) on the same scale.

(d) UV-vis spectroscopy

The diffuse reflectance spectra of the samples analysed are presented in Fig. 2. Titanium oxide presented the typical spectrum, absorption in the ultraviolet region (412 cm^{-1}). The absorption capacity is modified by the presence of gold particles (422 nm) compared to titanium oxide. Platinum also modifies the absorption capacity with respect to gold (470 nm). The sample impregnated with ruthenium showed a much higher absorption capacity (539 cm^{-1}) compared to AuTi and PtTi. The sample with rhodium shows a much higher absorption capacity compared to the other noble metals, absorbing in the visible region.[32] As for the localized surface plasmon resonance (LSPR),

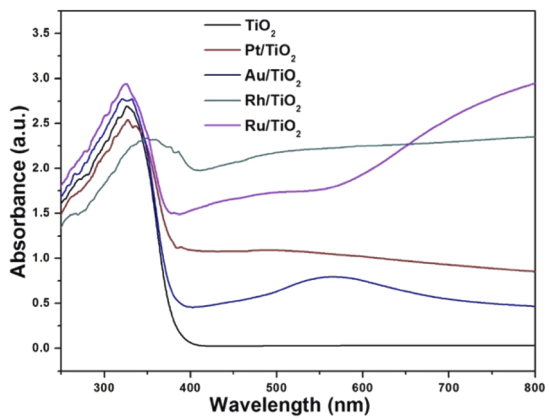

Fig. 2 UV-vis spectra of the photocatalysts.

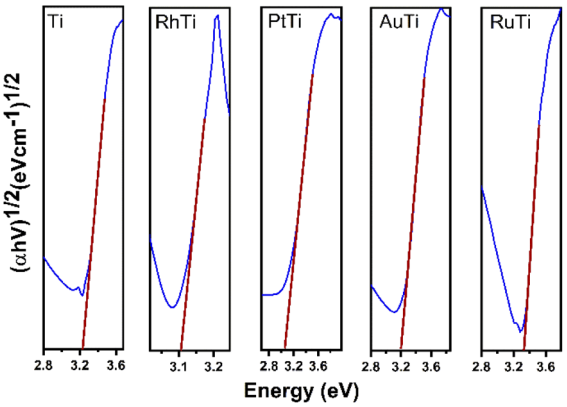

Fig. 3 Tauc plot of photocatalysts.

metallic gold is in the visible region (440–600 nm), an effect induced by nanoparticles on the surface of titanium oxide.[33] In the platinum sample the SPR is slightly detectable, this is due to the particle size present on the surface. The size of the metal particle is inversely proportional to the absorption of the surface plasmon resonance.[34] An absorption near 450 nm was observed in the sample, a signal assigned to localized surface absorption of the ruthenium plasmon.[35] In this sample, a broad absorption is observed in the 600–800 nm region, associated with the electromagnetic field-induced collective oscillation of free conduction electrons filling the states near the Fermi level in the conduction band.[36] Concerning the rhodium sample, theoretical studies indicate that Rh NPs have a very strong UV plasmonic response and show a local surface plasmon resonance near 330 nm.[37,38] It is well known that LSPRs depend on the size and shape of nanoparticles.[38] The results suggested that noble metal-loaded titanium can enhance the photocatalytic activity under visible light irradiation.

Fig. 3 shows the Tauc plot to determine the band gap energy (E_g) of the photocatalysts in this work. TiO_2 showed an energy of 3.24 eV. This result agrees with the literature of 3.2 eV. In the case of metal catalysts, it was 3.09, 3.10, 3.18 and 3.31 eV for PtTi, RhTi, AuTi and RuTi, respectively (Table 2). This decrease

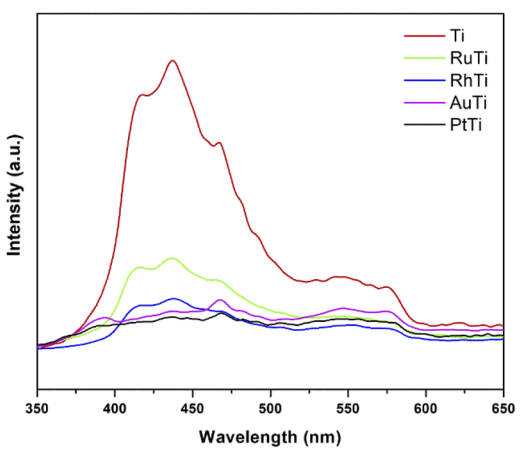

Fig. 4 Photoluminescence spectra of photocatalysts.

in bandgap energy is due to surface structural changes between TiO_2 and the metal. The modification in the Fermi level near the CB of the semiconductor helps to improve the useful life of the photogenerated electrons, which causes the decrease in the recombination of charge carriers, benefiting the photocatalysis process that occurs on the surface.[39,40] This effect is observed in the PL spectra (Fig. 4). Because a metal–semiconductor Schottky junction is formed, facilitating charge separation and transfer.[41]

(e) Solid fluorescence

To investigate the fate of photogenerated electrons as a function of noble metals as well as holes in semiconducting nanoparticles, photoluminescence analysis was employed. PL emission is the direct result of the recombination of free carriers.[42–45] The lower PL intensity is indicative of the lower recombination rate of photogenerated charge carriers Fig. 4 shows the results of irradiation at 310 nm and in a wavelength range of 300–700 nm. The peak associated with the band gap transition emission appears at 398 nm.[46] Emission signals at 420 and 440 nm should be attributed to indirect band gap and surface recombination.[47] Other emission peaks at about 480 and 520 nm are caused by O_2 vacancies and surface defects of the samples. Because the Fermi levels of metals (Rh, Ru, Pt and Au) are lower than the conduction band of titanium oxide, the photoexcited electrons can be transferred from the semiconductor to the metal nanoparticles deposited on the TiO_2 surface. According to the photoluminescence results, metals reduce the possibility of electron hole recombination. The signal intensity of titanium oxide is higher due to the higher rate of electron hole recomposition under irradiation. The maximum intensity of noble metals modified TiO_2 increased in the following order RuTi < RhTi < AuTi < PtTi.

(f) X-ray photoelectron spectroscopy (XPS)

Fig. 5 shows the XPS deconvoluted spectra of the metal species (Rh, Ru, Pt, Au) of the photocatalysts supported on TiO_2, synthesized by the impregnation method. Where the oxidation states of each of the photocatalysts are studied. According to the literature, rhodium presents a doublet due to the spin–orbital splitting in the $3d_{3/2}$ and $3d_{5/2}$ regions between the binding energy of 315–305 eV.[48] Rhodium can present two oxidation states Rh° (ref. 49) *y* Rh^{3+} between 306.8–307.1 and 307.7–308.5 eV respectively. In case of RhTi two oxidation states are observed at 306.7 and 307.8 eV for Rh° and Rh^{3+} respectively. According to Y. V. Larichev *et al.* mentions that titanium has surface properties that benefit the reduction to Rhodium metal using $RhCl_3$ precursor. Table 1 shows the percentage of abundance of the oxidation states where Rh° presents 54.4% and Rh^{3+} 45.6%, which means that there is a Rh°/Rh^{3+} ratio of 1.19. In the Ru 3d spectrum for RuTi, deconvolution was performed knowing that there is an overlap with the C 1s according to Lan Jiang *et al.* and Jingjing Tan *et al.*[50,51] where C 1s and C=O species were found between the binding energies 284.8 and 288.9 eV respectively. On the other hand, in the 3d5/2 region, two signals at approximately 280.2 and 281.6 eV are observed. The position at 280.2 is attributed to the metallic state of Ru° (ref. 32) and the one at 281.6 is attributed to the oxidized state of Ru^{4+}.[52] According to Table 2 shows a % species abundance 84.2 for the metallic state and 15.8% for the 4+ state. Weiyi Ouyang *et al.*[53] report that ruthenium can provide interesting activity due to the existence of plasmon resonances directly attributed by the Ru^{4+} oxidation state. Fig. 5 shows the binding energies for the Au 4f levels in the case of gold, the energies for the metallic state are at 84 eV and the oxidized Au^{+} species between 85.6–87.7 eV approximately according to the literature.[54] However, a peak at 83.3 eV was found at the $4f_{7/2}$ level, this result shows that there is a shift of $\Delta = 1.3$ eV with respect to the Au° characteristic signal. Different authors mention that this shift is caused by a strong metal–support interaction in this case the Au°–TiO_2 interaction.

On the other hand, no signal characteristic of Au^{+} was found. In the case of Pt deconvolution, it was carried out in the $4f_{7/2}$ region, where different platinum oxidation states were found: 70.74 eV (Pt°),[55] 73.0 eV (Pt^{2+})[56] *y* 75.0 eV (Pt^{4+})[57] with an abundance of 56.5, 24.9 years 18.7% respectively (Table 1). For the Ti 2p region in all the catalysts, two oxidation states Ti^{3+} and Ti^{4+} were found, where the deconvolution was carried out in the Ti

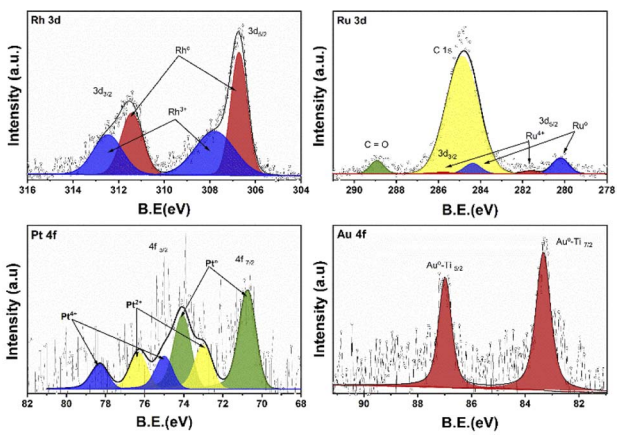

Fig. 5 XPS spectra of the Rh 3d, Ru 3d, Pt 4f and Au 4f regions of the RhTi, RuTi, PtTi and AuTi photocatalysts.

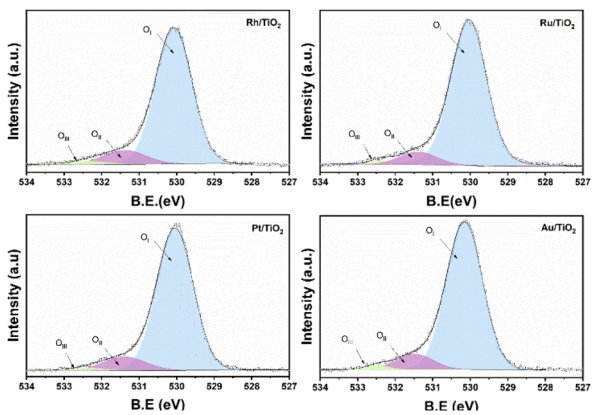

Fig. 6 XPS spectra of the O 1s region of the RhTi, RuTi, PtTi and AuTi photocatalysts.

$2p_{3/2}$ region (figure not shown) at 458.7 and 457.2 eV approximately. TiO_2 showed the lowest percentage of abundance of the Ti^{3+} species (Table 1) with 3.1%, on the other hand, the catalysts Rh, Ru and Pt showed an increase in percentage with respect to TiO_2, this increase is probably related to a strong metal–support interaction.[58] Fig. 6 shows the deconvolution of the O 1s spectra of the photocatalysts, where the superposition of three components was found at approximately 530.2, 531.5 and 532.5 eV. for O_I, O_{II} and O_{III}, respectively. The O_I peak is characteristic to the O^{2-} ions found in the surface lattice of TiO_2.[59] On the other hand, the O_{II} peak is attributed to oxygen defects in the TiO_2 matrix related to oxygen vacancies.[60] The anionic vacancies change the net electron charge density; this non-lattice oxygen peak has been attributed to the surface O^- ions with lower electron density.[61] The peak at 532.5 (O_{III}) is related to hydroxyl groups, in this case, to Ti–OH groups. According to Table 1, the abundances related to O_I are between 88 and 91% approximately. In the case of oxygen defects (O_{II}) on the TiO_2 surface, the RhTi and PtTi photocatalysts showed the highest percentage of abundance with 10.6 and 10.7% approximately. Likewise, the catalysts with Rh and PT showed the highest abundance attributed with the formation of Ti–OH groups. These results could be related to a better activity in the degradation of 2,4-D.

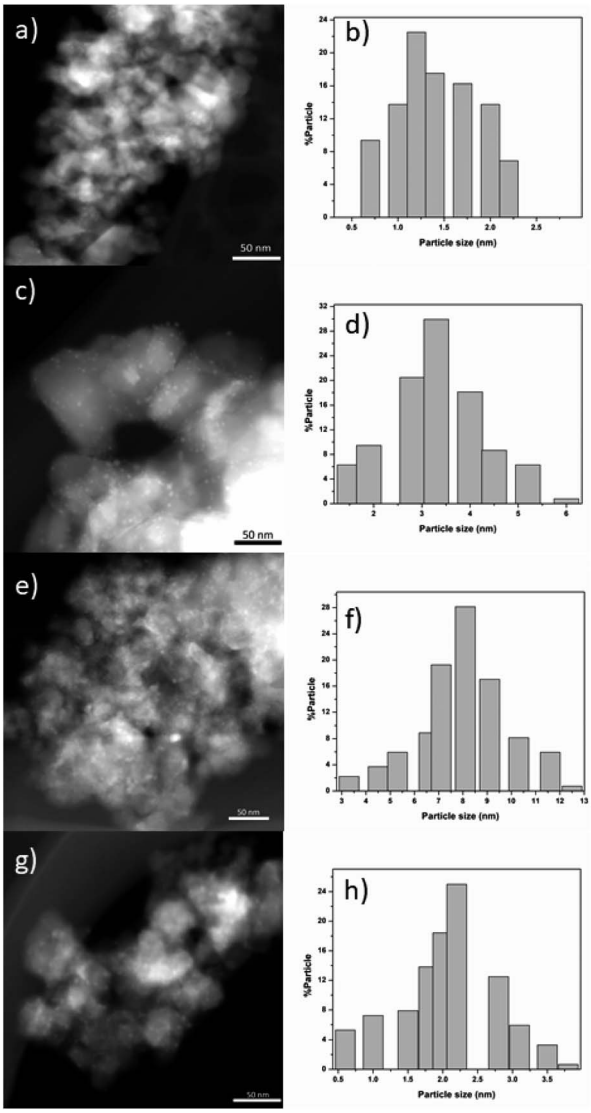

Fig. 7 HAADF images of RhTi (a), RuTi (c), PtTi (e) and AuTi (g). Histograms of the metal particle size of RhTi (b), RuTi (d), PtTi (f) and AuTi (h) catalysts.

(g) HAADF-STEM

Fig. 7 shows typical TEM-HAADF images showing metallic particles of RhTi, AuTi, RuTi and PtTi reduced at 500 °C. Table 2 shows the average sizes of the metallic particles calculated from the histograms, see Fig. 7. In HAADF mode, the image intensity is approximately proportional to the square of the atomic number of element (Z^2),[62] and due to the differences between Rh (45), Au (79), Ru (45), Pt (78) and Ti (22) values, Au and Pt particles provide higher contrast in TEM-HAADF images. Therefore, the highly contrasted particles can be attributed to metallic particles, with the AuTi and PtTi samples having larger size in the metallic particle (Fig. 7e and g). The metals with the lowest metal dispersion were Pt and Ru which according to the literature, the synthesis precursor directly influences the particle size of Ru.[63] While the Pt dispersion, due to its high content, presents large particle sizes in comparison with Rh, Ru and Au. According to the literature, concentrations higher than 1% of platinum generate particles larger than 5 nm.[64] In contrast, higher dispersion is present in Rh and Au metals. One of the characteristics of Rh metal is its ease of dispersion.[65] Despite the high Au content, it has been reported that using $HAuCl_4$ it is possible to obtain small metallic particles.[66]

(h) Quantification of radicals (OH)

According to sonochemistry when ultrasound is applied to water, $OH^{\bullet}$ $OH_2^{\bullet}$ O_2^- *y* H_2O_2 species can form because of the high energies generated during cavitational collapse.[67] These species can also be formed by chemical radiation, *via* an ionizing photon.[68] These species are similar to those produced in oxidation processes *via* photocatalysis.[69] In Fig. 8, the

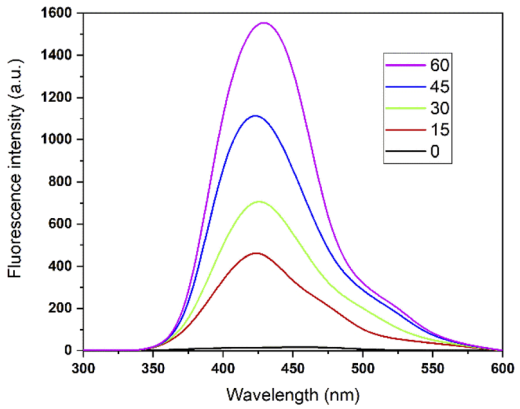

Fig. 8 Fluorescence spectra of PtTi.

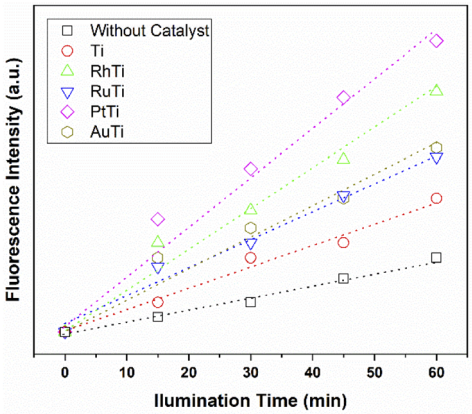

Fig. 9 Dependence of fluorescence intensity on illumination time.

fluorescence results of the PtTi catalyst are shown. The spectrum of the PtTi catalyst has the same shape and maximum emission wavelength with respect to that reported by Xiao *et al.*[70] Therefore, it is possible that the fluorescent products generated on the PtTi catalyst are a product of the reaction of terephthalate with OH˙ Fig. 9 shows the dependence of fluorescence intensity on illumination time at 425 nm. The intensity follows an almost linear trend, so the formation of OH radicals is proportional to the illumination time, obeying zero order kinetics. The lines that fit each series provide the slope, which can be related to the rate of formation of OH radicals,[70] see Fig. 9. The catalysts keep an order with respect to the rate of radical formation: PtTi > RhTi > AuTi > RuTi > Ti. In general, the incorporation of metal improves the formation rate of OH radicals, which indicates that the metals Pt and Rh present a better photoactivity in the oxidation reaction of 2,4-D.

(i) Photocatalytic activity

The conversion of the pollutant as a function of time for all catalysts is shown in Fig. 10. The incorporation of catalyst in the degradation increases the conversion, this can be verified by analysing the curve corresponding to the Ti sample and the uncatalyzed reaction. The RhTi sample showed a linear trend in 100 min of reaction, achieving 96.37% conversion in 120 min. The RuTi catalyst presented an almost linear progress, reaching 91.37% conversion at 150 min of reaction. The PtTi sample stands out for reaching 96.53% conversion in only 100 minutes. Finally, the AuTi sample presented a continuous and slightly superior behaviour with respect to the RuTi sample, without achieving 80.78% conversion in the established time. The rhodium metal showed to be active in photodegradation, obtaining good results compared to Ru and Au. Despite the high Pt content, the rhodium metal presents a convenient activity to highlight, demonstrating that it is a metal to be considered in the photodegradation of molecules.

As for the total degradation of the compound, the TOC analysis indicates (Fig. 11) that only the PtTi and RhTi catalysts destroy the pollutant around 97%. It should be noted that the PtTi sample degrades 96.53% of 2,4-D in 105 minutes and mineralize (S_{co_2}) 99.0% to CO_2. In this sense, the RhTi sample only take 15 minutes more than PtTi in both stages to 96.4 and 98.3% of degradation and mineralization respectively. Despite the photocatalytic activity presented by the RuTi catalyst, it's not exceeded 81% mineralization of 2,4-D did not manage to exceed 80% mineralization of 2,4-D. These results may be related to the formation of Ti^{3+} shown by the XPS results in the table, since according to Li *et al.* enhances oxygen chemisorption and promotes excited electrons trapped by O_2.[71]

Therefore, the enhancement of photoactivity has a good agreement with the decrease of PL intensity (Fig. 4).

The apparent kinetic constant and the half-life were calculated, assuming first-order,[72] the results are shown in Table 2. The value of the kinetic constant for the Ti sample is lower when compared to the samples with metal. An increase in the kinetic constant is evident when incorporating a noble metal, despite being the sample with the lowest value in the constant with respect to RhPt and Au, RuTi is 2.3 times higher than Ti. As for the highest values are the samples PtTi and RhTi, the difference between them is only 2.58%. The half-life indicates that in the absence of metal, at least 180 min must elapse to achieve 50% conversion. In contrast, the half-life is reduced by up to 68% for PtTi and 66% for RhTi taking Ti as a reference. In this respect, there is only a difference of 2 min between the RhT and PtTi samples. According to the metal particle size, the Rh showed

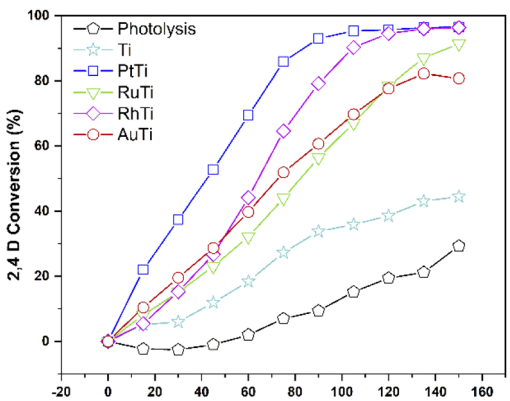

Fig. 10 2,4-D conversion monitored by UV.

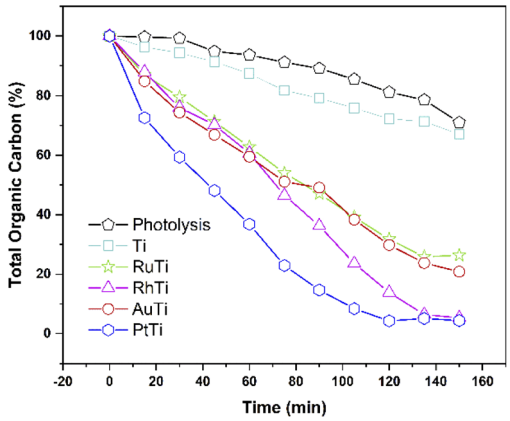

Fig. 11 Mineralization of the catalysts as a function of time.

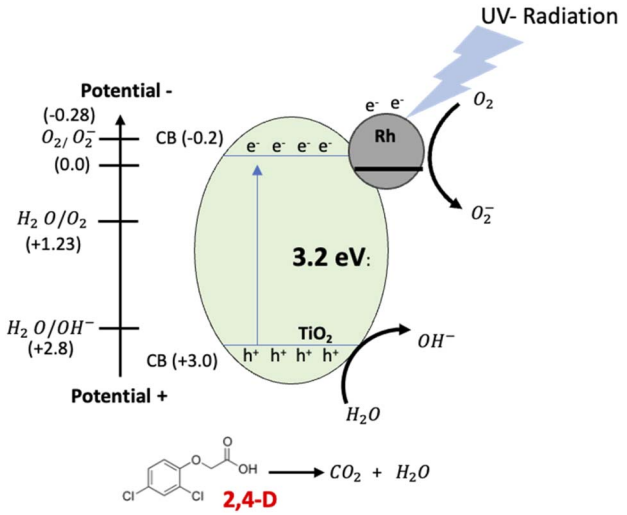

Fig. 12 Schematic representation of the proposed photocatalysis mechanism of 2,4-D degradation on the Rh/TiO_2 by UV radiation.

small metal particle size (1.6 nm) compared to the other metals and the highest dispersion with 69%. However, metal deposition changes the properties of the surface, reducing it because of the removal of oxygen atoms;[73] increasing vacancies. The main interaction is ionic attraction due to charge transfer between the reduced surface and the adjacent metal atoms.[58] Therefore, a reduction of the surface is essential to ensure good photoactivity in the degradation of pollutants. In this sense, it has been reported the importance of interaction that takes place between the metal Rh,[48] Ru,[74] Pt (ref. 75) and Au (ref. 76) with the vacancies of titanium oxide.

The materials with Pt and Rh were the best in the mineralization of 2,4-D, however, considering the metal load, the RhTi is better, because only 1% of metal load was used. According to the above in Fig. 12 shows of the RhTi mechanism photocatalytic, where the surface adsorbed O_2 molecules were reduced to form superoxide radicals (O^{2-}), which are unstable in aqueous solution and can be readily decomposed into hydroxyl radicals (OH^-) with sufficient oxidation potential for the photocatalytic degradation of recalcitrant compounds.[77,78] This effect is for the higher adsorption capability of O_2 on the surface of the anatase phase of TiO_2 and the Rh reduce the recombination rate for the electron–hole pairs photogenerated.[79] These hydroxyl radicals easily degrade the 2,4-D into CO_2 and H_2O. The generation of OH^- is an important key in the degradation of organic compounds, in this work, according to the quantification of OH^- (Fig. 9), a strong relationship was found, where the PtTi and RhTi catalysts showed greater generation of OH^-, in such a way that manner were the ones that best mineralized 2,4-D.

Accorded to above, several experiments with scavengers were carried out to confirm the species involved in the UV photocatalytic reaction with RhTi catalyst. Scavenger experiments were benzoquinone (BQ, superoxide anions O^{2-}), isopropanol (IPA, $^{\bullet}OH$ radicals), ethylenediaminetetraacetic acid (EDTA, h^+ hole trapping) and potassium dichromate ($K_2Cr_2O_7$, e^-).[80,81] Fig. 13 shows the results of the apparent kinetic constant after the addition of scavengers, where a decrease of 83 and 63% was obtained with IPA and BQ, respectively. This result shows that OH radicals and superoxide (O^{2-}) play a very important role in the photodegradation of 2,4D. On the other hand, a decrease of 14% and 21% was observed with $K_2Cr_2O_7$ and EDTA. this shows little contribution to degradation.

(j) Stability and recyclability reaction

It is important to carry out a study of the stability and reuse cycles of the catalyst to know if the catalyst can be promising and reduce costs in photocatalytic processes. Fig. 14 shows the reuse cycles of the RhTi catalyst. For each cycle, the catalyst was filtered, washed several times with methanol and dried at 120 °C. Finally, the catalyst was calcined in a flow of H_2 at 400 °C for 1 h. According to the results obtained, after 3 cycles of reuse, the catalyst had a loss of 7.7% of activity with respect to the fresh catalyst. This result showed that a very significant change in the reaction was not obtained.

On the other hand, after the reuse cycles, the XRD study was carried out (Fig. 15) to find out if there was a change in the

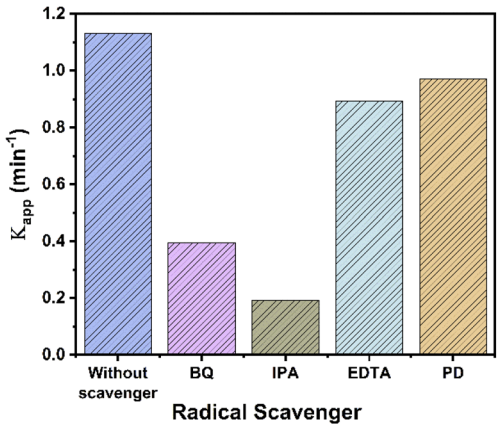

Fig. 13 Apparent kinetic constant (k_{app}) for the degradation of 2,4D by RhTi with and without different scavengers.

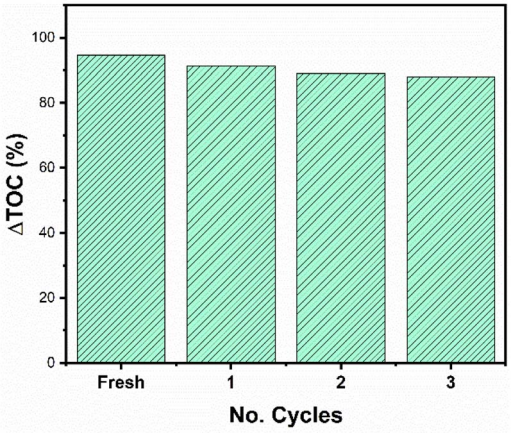

Fig. 14 Reuse cycles of RhTi catalyst of 2,4-D mineralization.

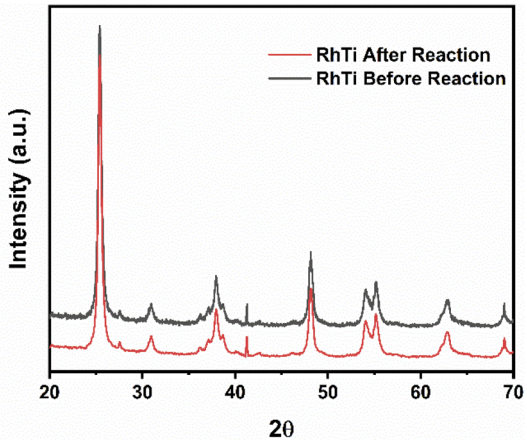

Fig. 15 XRD of RhTi: before and after cycles of 2,4-D mineralization.

material, however, no significant changes were found in the structure of the catalyst.

Experimental

(a) TiO_2 preparation

Titanium oxide was synthesized by the sol–gel method under the following procedure: *n*-titanium butoxide and *n*-butanol were placed in a balloon flask under constant stirring at pH 7. Subsequently, an alkoxide/water ratio of 1/8 was added dropwise. The system was kept under refluxing conditions for 24 hours at 70 °C. Afterwards, the excess solvents were removed using a rotary evaporator. The solid obtained was dried at 120 °C for 12 hours and then sieved to obtain a fine powder. Finally, the material was calcined at 500 °C for 12 hours using a heating rate of 2 °C min^{-1} under an air flow of 60 mL min^{-1}.

(b) Impregnation of metals (Au, Pt, Rh and Ru)

The precursor salts were $RhCl_3 \cdot xH_2O$, $RuCl_3 \cdot H_2O$, $H_2Cl_6Pt \cdot 6H_2O$ and $HAuCl_4 \cdot 6H_2O$. Rhodium was taken as a reference, therefore, as a comparison target the amount of Rh (1 wt%) in moles is the same in Ru (0.98 wt%), Pt (1.89 wt%) and Au (1.91 wt%). The required amount of salt was dissolved and introduced to a 250 mL balloon flask where titanium oxide was in suspension. The solvent was extracted in a rotary evaporator. Subsequently, the sample was placed in an oven at 120 °C for 24 hours. The sample received a heat treatment in an air flow at 60 mL min^{-1} with a heating ramp of 1 °C min^{-1} until reaching 500 °C. The metal was obtained in a thermal process in a reducing atmosphere (hydrogen) with a flow rate of 60 mL min^{-1} and a heating ramp of 1 °C min^{-1} until reaching 500 °C, remaining at that temperature for 5 hours. The following symbology was used: Ti for TiO_2 and XTi for impregnated TiO_2 where X = Ru, Rh, Pt and Au.

(c) Characterization

(c.1) BET specific surface area. The nitrogen adsorption process was determined on a Quantachrome Autosorb 3B analyzer. The analysis was carried out at −196 °C in liquid nitrogen; degassing was performed in vacuum at a temperature of 300 °C in gaseous nitrogen. The specific surface area was calculated using the equation proposed by Brunauer–Emmett–Teller (BET).

(c.2) X-ray diffraction. X-ray diffraction spectra were obtained at room temperature in a Bruker D8 Advance diffractometer, with a Cu-Kα radiation and with a monochromatic graphite secondary beam. The diffraction intensity, as a function of angle at 2θ, over a range from 10 to 70° with a step of 0.05° and a measurement time of 0.5 s per spot.

(c.3) UV-vis absorption spectra. UV-vis absorption spectra were determined on a Varian Cary-III UV-vis Spectrophotometer coupled to a diffuse reflectance integrating sphere. $BaSO_4$ was used as a reference for 100% reflectance. They were used to estimate the bandgap energy (E_g) of the catalysts, if the absorption coefficient (α) and the parameter A are equal to zero, with m equal to 1 according to equation:

$$\alpha(h\nu) = A(h\nu - E_g)^{m/2}$$

(c.4) X-ray photoelectron spectroscopy (XPS). Oxidation states and relative abundances were determined by the results obtained from a KRATOS Axis ULTRA X-ray photoelectron spectrometer, incorporated with a hemispherical analyser of electron energy of 165 mm. The incident radiation used was monochromatic Al Kα X-rays (1486.6 eV) at 225 W (15 kV, 15 mA). The pressure in the analysis chamber of samples was 1×10^{-8} torr. Data was analysed by XPS Casa software, version 2.3.14, and using as a reference carbon at 285.0 eV to adjust the peaks of the species studied.

(c.5) Solid fluorescence. The fluorescence spectra (emission) of the catalysts were analysed at a wavelength of 254 nm (wavelength radiated by the mercury lamp) in an ISS K2 fluorometer (Champaign, IL, USA).

(c.6) Quantification of radicals (OH). 150 mg of the photocatalyst was introduced to 200 mL of solution containing 5×10^{-4} M terephthalic acid (Aldrich 98%) and 2×10^{-3} M NaOH (Baker 97%) to ensure the solubility of the molecule.[82] The solution was continuously stirred; the system was irradiated with UV light for 1 h at room temperature (25 °C). Samples were taken at 0, 5, 10, 15, 15, 30, 45 and 60 min, were filtered using a 0.45 mm membrane. Fluorescence spectra of the terephthalic acid hydroxylation reaction were measured on an ISS K2 fluorometer (Champaign, IL, USA), with an emission wavelength of 425 nm and excitation wavelength of 315 nm. As an additional test, fluorescence measurements of the terephthalic acid solution irradiated with UV light in the absence of the photocatalyst were performed at the same times.

(c.7) ICP-analysis. Metal concentration was obtained by optical emission spectroscopy with inductive coupling plasma (ICP-OES) using a PerkinElmer 4200 DV equipment. For the preparation of the sample, 50 mg of catalyst were weighted and placed in a Teflon beaker, 3 mL of HF and 6 mL of a mixture of acid solution (4 mL of HNO_3 and 2 mL of HCl) were added. The mixtures were placed in an ultrasound bath at 75 °C for 1 h.

After digestion, the solutions were filtered and calibrated in flasks of 50 mL with double distilled water.

(c.8) HAADF-STEM. High Annular Angle Analysis Darkfield (HAADF) and Transmission Electron Microscopy Scanning (STEM) were performed on a JEOL JEM-2200FS Transmission Electron Microscope with an accelerating voltage of 200 kV and integrated with an ultra-high resolution Schottky-type field emission gun. The configuration used is Cs = 0.5 mm, Cc = 1.1 mm, dot by dot resolution of 0.19 nm and an omega-type column. For the analysis, the samples were pulverized, suspended, dispersed, and placed on copper grids (3 mm thick). The average metal particle size ($\bar{d}$) was calculated using equation:

$$\bar{d} = \frac{\sum_{i=1}^{n} n_i d_i^3}{\sum_{i=1}^{n} n_i d_i^2}$$

where d_i is the diameter measured directly from the image; and n_i is the number of particles having the same diameter d_i.

(d) Photocatalytic activity

Photodegradation was performed at room temperature for 150 min, according to the following methodology: 125 mg of catalyst was added to 200 mL of aerated solution with a 40 ppm contaminant concentration of 2,4D (dichlorophenoxyacetic Acid), bubbled with a pump (BOYU S-4000B, pressure 0.012 MPa, power 9 W and an output flow of 3.2 L min^{-1}) and constant agitation to achieve adsorption–desorption equilibrium. Subsequently, it was irradiated with a UV lamp (Pen-Ray (UVP), λ = 254 nm and an emission of 4000 μW cm^{-2}), all this in the absence of light. From the reaction, samples were taken every 15 min and the evolution of the photodegradation was followed by an Agilent Technologies UV-vis spectrophotometer, model Cary 60, monitoring the intensity of the absorption band of 2,4-D at 282 nm (applying the Lambert–Beer equation) as a function of irradiation time. Photolysis of 2,4-D was also performed in the complete absence of light and without catalyst. All photocatalytic evaluations were performed in duplicate. The % conversion of 2,4D ($X_{2,4D}$) was calculate with the equation:

$$X_{2,4D} = \frac{C_0 - C_n}{C_0} \times 100\%$$

where C_0 is an initial concentration of 2,4D and C_n is the 2,4D concentration to different reaction times.

Total Organic Carbon analysis (TOC), a Shimadzu TOC-VCHS analyser was used to obtain this parameter, employing a nondispersive infrared detector to quantitatively analyse carbon dioxide originated by the sample. The % TOC was calculated with the equation:

$$\%\mathrm{TOC} = \frac{\mathrm{TOC}_0 - \mathrm{TOC}_t}{\mathrm{TOC}_0} \times 100\%$$

where TOC_0 is total organic carbon at $t = 0$ and TOC_t is total organic carbon at different time in the oxidation reaction. The selectivity to CO_2 was calculated according to follow equation:

$$S_{CO_2} = \frac{\%\mathrm{TOC}}{X_{2,4D}} \times 100\%$$

Conclusions

In this research work, the comparison of Rh on TiO_2 was carried out, with respect to Pt, Au and Ru. Where the PtTi and RhTi showed the better photocatalytic properties because the decrease in bandgap energy (E_g), which generated a strong support–metal interaction which caused the decrease in the recombination of charge carriers, benefiting the photocatalysis process that occurs on the surface. Consequently, showing a good activity in the degradation and mineralization of 2,4-D. The PtTi catalyst showed a higher activity, but not very significant, with a difference of 2.85% in the reaction rate constant. However, RhTi achieved this photocatalytic process with a lower amount of by weight (1 wt%), a smaller metal particle diameter and a higher metal dispersion. On the other hand, the Ru and Au catalysts did not show good activity when compared to Rh. This results as a reference point to continue research the photocatalytic degradation of another organic compounds using $RhTiO_2$ photocatalyst.

Author contributions

G. A. Reguero-Márquez: methodology, software, validation, formal analysis, investigation, writing-original draft, writing-review & editing, visualization. Ma. A. Lunagómez-Rocha: methodology, software, validation, formal analysis, investigation, writing-original draft, writing-review & editing, visualization, project administration, funding acquisition. A. Cervantes-Uribe: methodology, validation, investigation, writing-original draft, writing-review & editing, visualization, project administration, funding acquisition. G. del Angel: investigation, writing-original draft, writing-review & editing, visualization. I. Rangel: investigation, writing-original draft, writing-review & editing, visualization. J. G. Torres Torres: conceptualization, methodology, validation, formal analysis, investigation, resources, writing-original draft, writing-review & editing, visualization, supervision, project administration, funding acquisition. F. González: investigation, writing-original draft, writing-review & editing. S. Godavarthi: investigation, writing-original draft, writing-review & editing, visualization. J. C. Arévalo-Pérez: methodology, validation, investigation, writing-original draft, writing-review & editing, visualization. A. E. Espinosa de los Monteros: investigation, writing-original draft, writing-review & editing, visualization. A. A. Silahua-Pavon: methodology, software, validation, formal analysis, investigation, writing-original draft, writing-review & editing, visualization, project administration, funding acquisition.

Conflicts of interest

There are no conflicts to declare.

Acknowledgements

We would like to thank the National Council of Science and Technology (CONACYT), Project No. 132648, Cátedras CONACYT (Invesigadoras e Investigadores por México) Project Number 1024 "Nanomaterials Study to Energy Applications", PRODEP project with codes UJAT-PTC-250, 287 and finally the SEP-PFCE-UJAT-DACB 2020-2021 program project for their financial support.

References

1 J. Popp, K. Pető and J. Nagy, *Agron. Sustainable Dev.*, 2013, **33**, 243–255.
2 W. Yang, F. Jiao, L. Zhou, X. Chen and X. Jiang, *Appl. Surf. Sci.*, 2013, **284**, 692–699.
3 D. H. Garabrant and M. A. Philbert, Review of 2,4-Dichlorophenoxyacetic Acid (2,4-D) Epidemiology and Toxicology, *Crit. Rev. Toxicol.*, 2002, **32**(4), 233–257.
4 D. J. Hamilton, Á. Ambrus, R. M. Dieterle, A. S. Felsot, C. A. Harris, P. T. Holland, A. Katayama, N. Kurihara, J. Linders, J. Unsworth and S. Wong, *International union of pure and applied chemistry and the environment division commission on agrochemicals and the environment* regulatory limits for pesticide residues in water (Iupac Technical Report)*, Japan, 2003, vol. 75.
5 *DOF - Diario Oficial de la Federación*, **https://www.dof.gob.mx/nota_detalle.php?codigo=2063863&fecha=31/12/1969#gsc.tab=0**, (accessed September 6, 2022).
6 *DOF - Diario Oficial de la Federación*, **https://www.dof.gob.mx/nota_detalle.php?codigo=5603318&fecha=22/10/2020#gsc.tab0**, (accessed September 6, 2022).
7 V. O. Njoku, K. Y. Foo and B. H. Hameed, *Chem. Eng. J.*, 2013, **215–216**, 383–388.
8 J. S. Valente, F. Tzompantzi, J. Prince, J. G. H. Cortez and R. Gomez, *Appl. Catal., B*, 2009, **90**, 330–338.
9 A. J. González, A. Gallego, V. L. Gemini, M. Papalia, M. Radice, G. Gutkind, E. Planes and S. E. Korol, *Int. Biodeterior. Biodegrad.*, 2012, **66**, 8–13.
10 A. Fujishima, T. N. Rao and D. A. Tryk, Titanium dioxide photocatalysis, *J. Photochem. Photobiol., C*, 2000, **1**(1), 1–21.
11 W. Wen, J. Hai, J. Yao, Y.-J. Gu, H. Kobayashi, H. Tian, T. Sun, Q. Chen, P. Yang and C. Geng, *Chem. Mater.*, 2021, **33**, 1489–1497.
12 W. Wen, J.-M. Wu, Y.-Z. Jiang, L.-L. Lai and J. Song, *Chem*, 2017, **2**, 404–416.
13 C. Geng, T. Sun, Z. Wang, J.-M. Wu, Y.-J. Gu, H. Kobayashi, P. Yang, J. Hai and W. Wen, *Nano Lett.*, 2021, **21**, 7021–7029.
14 W. Choi, A. Termin and M. R. Hoffmann, The Role of Metal Ion Dopants in Quantum-Sized TiO_2: Correlation between Photoreactivity and Charge Carrier Recombination Dynamics, *J. Phys. Chem.*, 2002, **98**(51), 13669–13679.
15 U. G. Akpan and B. H. Hameed, *Appl. Catal., A*, 2010, **375**, 1–11.
16 J. C. Colmenares, M. A. Aramendía, A. Marinas, J. M. Marinas and F. J. Urbano, *Appl. Catal., A*, 2006, **306**, 120–127.
17 H. Katsumata, M. Sada, Y. Nakaoka, S. Kaneco, T. Suzuki and K. Ohta, *J. Hazard. Mater.*, 2009, **171**, 1081–1087.
18 S. Saha, J. M. Wang and A. Pal, *Sep. Purif. Technol.*, 2012, **89**, 147–159.
19 A. Ayati, A. Ahmadpour, F. F. Bamoharram, B. Tanhaei, M. Mänttäri and M. Sillanpää, *Chemosphere*, 2014, **107**, 163–174.
20 M. Gar Alalm, S. Ookawara, D. Fukushi, A. Sato and A. Tawfik, *J. Hazard. Mater.*, 2016, **302**, 225–231.
21 S. Sakthivel, M. v. Shankar, M. Palanichamy, B. Arabindoo, D. W. Bahnemann and V. Murugesan, *Water Res.*, 2004, **38**, 3001–3008.
22 S. Oros-Ruiz, R. Zanella and B. Prado, *J. Hazard. Mater.*, 2013, **263**, 28–35.
23 Y.-A. Chen, Y.-T. Wang, H. S. Moon, K. Yong and Y.-J. Hsu, *RSC Adv.*, 2021, **11**, 12288–12305.
24 C. C. Nguyen, C. T. Dinh and T. O. Do, *RSC Adv.*, 2017, **7**, 3480–3487.
25 B. Zhou, Y. Li, J. Bai, X. Li, F. Li and L. Liu, *Appl. Surf. Sci.*, 2019, **464**, 115–124.
26 L. Xiu-Hua, M. Dan and D. Yi, *Effects of rhodium doping on the microstructures and photocatalytic performances of TiO2 powders*, 2016, **40**(11), 678–682.
27 S. O. Sanni and O. G. Idemudia, *J. Nanomater.*, 2014, **2014**, 287493.
28 Y.-H. Chiu, K.-D. Chang and Y.-J. Hsu, *J. Mater. Chem. A*, 2018, **6**, 4286–4296.
29 M.-Y. Kuo, C.-F. Hsiao, Y.-H. Chiu, T.-H. Lai, M.-J. Fang, J.-Y. Wu, J.-W. Chen, C.-L. Wu, K.-H. Wei and H.-C. Lin, *Appl. Catal., B*, 2019, **242**, 499–506.
30 S. K. Dutta, S. K. Mehetor and N. Pradhan, *J. Phys. Chem. Lett.*, 2015, **6**, 936–944.
31 H. W. Chen, Y. Ku and Y. L. Kuo, *Water Res.*, 2007, **41**, 2069–2078.
32 E. Grabowskaa, M. Diak, T. Klimczuk, W. Lisowski and A. Zaleska-Medynska, *Mol. Catal.*, 2017, **434**, 154–166.
33 M. Scarisoreanu, A. G. Ilie, E. Goncearenco, A. M. Banici, I. P. Morjan, E. Dutu, E. Tanasa, I. Fort, M. Stan, C. N. Mihailescu and C. Fleaca, *Appl. Surf. Sci.*, 2020, **509**, 145217.
34 C. Langhammer, Z. Yuan, I. Zorić and B. Kasemo, *Nano Lett.*, 2006, **6**, 833–838.
35 X. Lin, K. Yang, R. Si, X. Chen, W. Dai and X. Fu, *Appl. Catal., B*, 2014, **147**, 585–591.
36 R. A. Ganeev, G. S. Boltaev, R. I. Tugushev and T. Usmanov, *Appl. Phys. B*, 2010, **100**, 571–576.
37 A. M. Watson, X. Zhang, R. Alcaraz De La Osa, J. M. Sanz, F. González, F. Moreno, G. Finkelstein, J. Liu and H. O. Everitt, *Nano Lett.*, 2015, **15**, 1095–1100.
38 M. Moskovits, *Surface-enhanced spectroscopy*, 1985.
39 M. M. Khan, S. A. Ansari, J. Lee and M. H. Cho, *J. Ind. Eng. Chem.*, 2013, **19**, 1845–1850.
40 X. Li, T. Fan, H. Zhou, B. Zhu, J. Ding and D. Zhang, *Microporous Mesoporous Mater.*, 2008, **116**, 478–484.
41 S. K. Khore, S. R. Kadam, S. D. Naik, B. B. Kale and R. S. Sonawane, *New J. Chem.*, 2018, **42**, 10958–10968.

42 D. Li, H. Haneda, S. Hishita and N. Ohashi, *Chem. Mater.*, 2005, **17**, 2596–2602.
43 Z. Bian, J. Zhu, F. Cao, Y. Lu and H. Li, *Chem. Commun.*, 2009, 3789–3791.
44 Y. Yang, Y. Yao, L. He, Y. Zhong, Y. Ma and J. Yao, *J. Mater. Chem. A*, 2015, **3**, 10060–10068.
45 Y. Cao, L. Zong, Q. Li, C. Li, J. Li and J. Yang, *Appl. Surf. Sci.*, 2017, **391**, 311–317.
46 M. V. Sofianou, N. Boukos, T. Vaimakis and C. Trapalis, *Appl. Catal., B*, 2014, **158–159**, 91–95.
47 J. C. Yu, J. Yu, W. Ho, Z. Jiang and L. Zhang, *Chem. Mater.*, 2002, **14**, 3808–3816.
48 J. Zhang, S. Liu, Q. Wang, J. Yao, Y. Liu and B. Liu, *Mater. Lett.*, 2020, **276**, 128257.
49 Y. v. Larichev, O. v. Netskina, O. v. Komova and V. I. Simagina, *Int. J. Hydrogen Energy*, 2010, **35**, 6501–6507.
50 L. Jiang and G. Zhou, *Appl. Surf. Sci.*, 2021, **535**, 147709.
51 J. Tan, J. Cui, X. Cui, T. Deng, X. Li, Y. Zhu and Y. Li, *ACS Catal.*, 2015, **5**, 7379–7384.
52 J. H. Shin, G. J. Kim and S. C. Hong, *Appl. Surf. Sci.*, 2020, **506**, 144906.
53 W. Ouyang, M. J. Muñoz-Batista, A. Kubacka, R. Luque and M. Fernández-García, *Appl. Catal., B*, 2018, **238**, 434–443.
54 N. Kruse and S. Chenakin, *Appl. Catal., A*, 2011, **391**, 367–376.
55 M. A. Matin, E. Lee, H. Kim, W. S. Yoon and Y. U. Kwon, *J. Mater. Chem. A*, 2015, **3**, 17154–17164.
56 D. A. Svintsitskiy, L. S. Kibis, A. I. Stadnichenko, E. M. Slavinskaya, A. S. Zaguzin, A. v. Romanenko, E. A. Derevyannikova, O. A. Stonkus and A. I. Boronin, in *AIP Conference Proceedings*, American Institute of Physics Inc., 2019, vol. 2143.
57 A. Romanchenko, M. Likhatski and Y. Mikhlin, *Minerals*, 2018, **8**, 578.
58 S. J. Tauster, S. C. Fung, R. T. K. Baker and J. A. Horsley, *Science*, 1981, **211**, 1121–1125.
59 K. Batalović, N. Bundaleski, J. Radaković, N. Abazović, M. Mitrić, R. A. Silva, M. Savić, J. Belošević-Čavor, Z. Rakočević and C. M. Rangel, *Phys. Chem. Chem. Phys.*, 2017, **19**, 7062–7071.
60 G. Cuauhtémoc, G. Torres and V. Bertin, *Catal. Today*, 2008, **133**, 588–593.
61 C. Mateos-Pedrero, S. R. González-Carrazán, M. A. Soria and P. Ruíz, *Catal. Today*, 2013, **203**, 158–162.
62 L. A. Calzada, C. Louis, C. W. Han, V. Ortalan and R. Zanella, *Appl. Catal. B*, 2020, **264**, 118503.
63 J. Okal, M. Zawadzki, P. Kraszkiewicz and K. Adamska, *Appl. Catal., A*, 2018, **549**, 161–169.
64 M. A. L. Rocha, G. del Ángel, G. Torres-Torres, A. Cervantes, A. Vázquez, A. Arrieta and J. N. Beltramini, *Catal. Today*, 2015, **250**, 145–154.
65 A. Cervantes, G. del Angel, G. Torres, G. Lafaye, J. Barbier, J. N. Beltramini, J. G. Cabañas-Moreno and A. Espinosa De Los Monteros, *Catal. Today*, 2013, **212**, 2–9.
66 H. Lihui, X. Songhai and L. Honglai, *Chin. J. Chem. Eng.*, 2007, **15**, 507–511.
67 X. Fang, G. Mark and C. von Sonntag, *Ultrason. Sonochem.*, 1996, **3**, 57–63.
68 K. Gopakumar, U. R. Kini and S. C. Ashawa, *Radiat. Eff.*, 1977, **32**, 199–203.
69 J. Peral, J. Casado and J. Doménech, *J. Photochem. Photobiol., A*, 1988, **44**, 209–217.
70 Q. Xiao, Z. Si, J. Zhang, C. Xiao and X. Tan, *J. Hazard. Mater.*, 2008, **150**, 62–67.
71 F. Li and X. Li, *Chemosphere*, 2002, **48**, 1103–1111.
72 C. S. Yang, Y. J. Wang, M. S. Shih, Y. T. Chang and C. C. Hon, *Appl. Catal., A*, 2009, **364**, 182–190.
73 R. Baker, E. Prestridge and L. Murrell, *J. Catal.*, 1983, **79**, 348–358.
74 G. Zhou, F. Wang and R. Shi, *J. Catal.*, 2021, **398**, 148–160.
75 Z. Chen, L. Liang, H. Yuan, H. Liu, P. Wu, M. Fu, J. Wu, P. Chen, Y. Qiu and D. Ye, *Appl. Catal. B*, 2021, **298**, 120507.
76 S. Chenakin and N. Kruse, *J. Catal.*, 2018, **358**, 224–236.
77 S. A. Ansari, M. M. Khan, M. O. Ansari and M. H. Cho, *New J. Chem.*, 2015, **39**, 4708–4715.
78 T. Bhowmik, M. K. Kundu and S. Barman, *RSC Adv.*, 2015, **5**, 38760–38773.
79 D. E. Juárez-Cortazar, J. G. Torres-Torres, A. Hernandez-Ramirez, J. C. Arévalo-Pérez, A. Cervantes-Uribe, S. Godavarthi, A. E. E. de los Monteros, A. A. Silahua-Pavón and A. Cordero-Garcia, *Water*, 2022, **14**, 1389.
80 Z. Hu, X. Cai, Z. Wang, S. Li, Z. Wang and X. Xie, *J. Hazard. Mater.*, 2019, **380**, 120812.
81 I. Cristea, A. Sobetkii, L. A. Constantin, M. A. Constantin and I. Nitoi, *Rev. Chim.*, 2020, **71**, 347–355.
82 K. Bubacz, E. Kusiak-Nejman, B. Tryba and A. W. Morawski, *J. Photochem. Photobiol., A*, 2013, **261**, 7–11.